Permeability evolution in fine-grained Aji granite during triaxial compression experiments

Kazumasa Sueyoshi[1]*, Ikuo Katayama[2] and Kazuki Sawayama[1]

[1]Institute for Geothermal Sciences, Graduate School of Science, Kyoto University

3088-176, Noguchibaru, Beppu, Oita, Japan, 874-0903

[2]Department of Earth and Planetary Systems Science, Hiroshima University

1-3-1 Kagamiyama, Higashi-Hiroshima, Japan, 739-8526

*corresponding author: Kazumasa Sueyoshi

Institute for Geothermal Sciences, Graduate School of Science, Kyoto University

3088-176, Noguchibaru, Beppu, Oita, Japan, 874-0903

E-mail: sueyoshi.kazumasa.3k@kyoto-u.ac.jp

Abstract

Triaxial compression experiments were carried out on samples of fine-grained Aji granite to measure the evolution of permeability during deformation prior to failure under confining pressures of 20 and 40 MPa. During the initial stages of deformation, a small decrease in permeability was observed, due to the closure of pre-existing microcracks; permeability then increased with increasing differential stress. During deformation, permeability varied by up to two orders of magnitude, and we observed a small pressure dependence, with a larger variation observed at 20 MPa than at 40 MPa. This suggests that more cracks developed during brittle deformation under the lower confining pressure. The observed increase in permeability during our experiments was approximately proportional to inelastic volumetric strain, which corresponded to the volume of dilatant cracks. On the other hand, prior to brittle failure we observed a further increase in permeability that was greater than the inelastic volumetric strain, suggesting crack aperture opening accelerated at this stress level (>~80%).

Keywords

Permeability and porosity, Microstructure, Fracture and flow, Geomechanics

1. Introduction

Fluid flow in rocks plays a key role in various geological processes, including crustal deformation (Byerlee 1975; Sibson 1996), fluid-induced seismicity (Talwani and Acree 1984), and geothermal developments (Shapiro et al. 1997). Laboratory experiments on rock samples have yielded a wide range of permeabilities (10^{-12} to 10^{-23} m^2) that are controlled by lithology, porosity and pore geometry (Gueguen and Palciauskas 1994). Under hydrostatic conditions, an increase in pressure reduces permeability through the progressive closure of pores within a rock (Brace et al. 1968; Fortin et al. 2011). During deformations of porous rocks such as sandstone, permeability consistently decreases due to the inelastic compaction through grain crushing and pore collapse (Zhu and Wong 1997; Baud et al. 2012). In contrast, brittle deformation of crystalline rocks such as granite can rapidly enhance permeability and affect fluid flow processes. Although a small decrease in permeability occurs upon the application of small stresses., a further increase in stress results in a marked increase in permeability as the rock approaches failure (Zoback and Byerlee 1975; Mitchell and Faulkner 2008). These stress-induced permeability variations are accompanied by dilatancy related to microcrack nucleation and growth. Therefore, the development of microcracks during deformation is of great importance in characterizing subsurface fluid flow.

In previous experiments, permeability was measured using the pulse transient technique, which requires the interruption of deformation to make measurements (Zoback and Byerlee 1975). This may induce a relaxation of the axial loading stress and the permeability may be affected, particularly during the dilatant stage. Mitchell and Faulkner (2008) measured the permeability evolution of Westerly granite during continuous triaxial compression using the pressure oscillation technique with water as a pore fluid. However, the high fluid viscosity required a relatively large response time to achieve equilibrium of permeability during deformation. In the present study, we measure permeability continuously during triaxial

compression using a gas flow method, in which the flux of gas, which is sensitive to the presence of deformation microstructures, was monitored. We used nitrogen gas because it is chemically inert, thereby preventing geochemical interaction and ensuring that the observed variation in permeability results exclusively from mechanical processes.

2. Experimental methods

For our experiments, we used sample of fine-grained granite from Aji, Japan. The average grain size of Aji granite is 0.3 mm, and it comprises 30 % quartz, 37 % plagioclase, 24 % K-feldspar, and 8 % biotite (Kudo et al. 1992). The samples have a bulk density of 2.66 g/cm^3 and an apparent initial porosity of 0.62 % (Yukutake 1989). Based on elastic wave velocity measurements, textures within the Aji granite are regarded to be near-isotropic (Watanabe and Higuchi 2015). Each sample was prepared as a cylindrical shape with a diameter of 20 mm and a length of 40 mm (uncertainty <0.05 mm). The samples were then enclosed in polyolefin tubes to prevent interaction with the confining oil.

Triaxial deformation tests were performed using an intra-vessel deformation fluid-flow apparatus at Hiroshima University. The axial piston was advanced at a constant rate and the confining pressure was kept constant using a servo-controlled system (Fig. 1). We performed multiple experiments under confining pressures of 20 and 40 MPa, and displacement rates of 0.04 and 0.02 mm/min. Our machine lacks a high-resolution feedback system to control post-failure processes, and we therefore focus on the evolution of permeability until the attainment of maximum differential stress.

Permeability was measured during deformation by a gas flow method using nitrogen gas as a pore fluid, in which a constant upstream pore pressure was maintained (P_p = 1.5 MPa). To achieve steady-state fluid flow during the initial stages of deformation, the desired pore pressure was applied an hour before the deformation was conducted. Permeability (k) was determined

from the flow rate as follows:

$$k = \frac{\mu}{A}\frac{L}{P_1 - P_2}\bar{Q}\,, \tag{1}$$

where μ is the viscosity of the pore fluid, P_1 is the upstream pore pressure, P_2 is the downstream pore pressure (atmospheric pressure), A and L are the cross-sectional area and length of the sample, respectively, and $\bar{Q}$ is the mean flow rate as measured by a digital flow meter (Tanikawa et al. 2008). During these calculations, we applied a correction to the pore fluid volume to account for the compressibility of nitrogen gas. Although changes in gas flow rate occur adjacent to pore walls, which results in pore pressure dependent permeability (i.e., Klinkenberg effect), we focus on the relative change in gas permeability under a constant pore pressure gradient.

We measured strain in sample during deformation using double-cross strain gauges. Volumetric strain (ε_v) was obtained from the axial (ε_a) and lateral strain (ε_r) as follows:

$$\varepsilon_v = \varepsilon_a + 2\varepsilon_r\,. \tag{2}$$

During the initial stages of deformation, volumetric strain varied linearly with applied differential stress. However, at stresses approaching the strength of the sample, non-linear behavior was observed during dilation of the samples due to the development of microcracks. As transport properties are influenced by the formation and connection of pores, we discuss the relationship between permeability and inelastic volumetric strain during deformation.

3. Results

Experimental conditions and results are listed in Table 1. Permeabilities prior to deformation ranged from 1.1×10^{-19} m^2 to 2.6×10^{-19} m^2, showing a small pressure dependence, with higher permeabilities observed at the lower confining pressure (20 MPa).

Figure 2 shows stress-strain curves for experiments conducted under confining pressures

of 20 and 40 MPa. We use positive strain to represent compression and negative for extension. The maximum differential stress varied with confining pressure, with experiments at high confining pressure (40 MPa) producing higher differential stresses than those at 20 MPa. Under both confining pressures, stress-strain behavior was linear-elastic during the initial stages of deformation and became non-linear under higher differential stress. This non-linear relationship prior to failure is typical behavior during brittle deformation, and reflects the development of microcracks in the samples. This process is referred to as dilatancy, and the volume is observed to increase during inelastic deformation. We determined the onset of dilatancy by following the method of Brace et al. (1966). The results indicate that dilatancy began at ~40% of the maximum differential stress, above which inelastic volumetric strain increased further as the stress increased. When approaching macroscopic failure, a reversal of stress–volumetric strain curve was observed at the stress level 62–77% of the maximum value. This stress threshold (termed "crack damage stress") corresponds to the point of the maximum volumetric strain where unstable crack growth initiates (Bieniawski, 1967).

Figure 3 shows permeability results for our experiments under confining pressures of 20 and 40 MPa. In all experiments, permeability initially decreased due to the closure of pre-existing cracks, and then increased under higher differential stress. Approaching the maximum differential stress, a more pronounced increase in permeability was observed. At the maximum differential stress, permeabilities were 0.4–2.3 $\times$ 10^{-17} m^2 and 1.6–3.9 $\times$ 10^{-18} m^2 at 20 and 40 MPa, respectively, and the maximum increase in permeability during deformation was approximately two orders of magnitude. The variation in permeability was larger at 20 MPa than at 40 MPa. Although most experiments were conducted at a constant displacement rate of 0.04 mm/min (strain-rate of ~1.7 $\times$ 10^{-5} s^{-1}), some runs were conducted at a slower rate of 0.02 mm/min; these experiments showed a similar evolution of permeability (Fig. 2). After reached the maximum differential stress, permeability continued to increase until macroscopic

failure. However, quantitative measurement of this stage was prevented because the axial load was not controlled by a servo-system, and brittle fracture occurred rapidly.

4. Discussion

4.1. Comparison with previous experiments

Our experiments yielded systematic changes in permeability during brittle deformation, and we first compare our results with previous experiments. Pioneering experiments by Zoback and Byerlee (1975) investigated the permeability evolution during triaxial deformation of Westerly granite samples. During loading, their results are similar to those presented here (Fig. 4a). However, their experiments were cycled and did not reach macroscopic failure, and hence variations in permeability were limited to a factor of four, much less than those found in our experiments until failure occurred. Mitchell and Faulkner (2008) measured the permeability of Westerly granite samples using a pore pressure oscillation technique at effective confining pressures of 10, 15, and 20 MPa. They observed a continuous increase in permeability after reaching approximately half of the maximum differential stress; however, in contrast to our experiments, an initial transient decrease in permeability related to the closure of pre-existing cracks was not clearly observed (Fig. 4b). This difference likely resulted from their use of water as a pore fluid, which has a higher viscosity than nitrogen gas, thereby limiting flow through the narrow cracks during initial stage of loading. Fortin et al. (2011) reported similar behavior during triaxial deformation of basaltic rocks (an initial decrease in permeability followed by an increase approaching failure), but the variation was less than a factor of three, likely due to competition between the closure of pre-existing cracks and the nucleation and growth of newly formed vertical cracks.

4.2. Relationship between permeability and inelastic volumetric strain

157 The inelastic behavior of the stress–volumetric strain relationship (i.e., dilatancy) initiates
158 ~40% of the maximum stress (C' in Fig. 5). As this dilatancy is related to the development of
159 microcracks, the increasing crack volume could enhance transport properties including
160 permeability. To explore the possible relationship between dilatancy and permeability during
161 deformation, we evaluated inelastic volumetric strain (D in Fig. 5) by subtracting an elastic
162 extrapolation from the measured volumetric strain.

163 Figure 6 shows the relative change in permeability and dilatancy as a function of the stress
164 level normalized by the maximum value. Permeability decreased slightly during the early stages
165 of deformation, and then began to increase at approximately half of the maximum differential
166 stress. This increase in permeability was accompanied by an increase in inelastic volumetric
167 strain. The change in permeability during this stage is attributed primarily to an increase in
168 dilatant crack porosity, considering that the inelastic volumetric strain corresponds to the crack
169 porosity. However, as samples approached brittle failure, permeability increased more rapidly
170 than inelastic volumetric strain. The differential stress at which the change in permeability
171 deviates from that of inelastic volumetric strain ~70–80% of the maximum stress. Therefore,
172 we infer that although permeability depends primarily on crack porosity, it is also influenced
173 by geometric factors (i.e., crack aperture) (Gueguen and Dienes, 1989; Sueyoshi et al., 2020).

174 One possible approach to estimating the contribution of crack geometric characteristics to
175 permeability is to clarify the power law between permeability (k) and porosity (φ) (Bernabe et
176 al., 2003):

177 $$k \propto \phi^{\alpha}. \quad (3)$$

178 The slope α depends on the processes that lead to the evolution of the pore structure, and lies
179 between 1 and 2 during dilatant microcracking. According to Bernabe et al. (2003), this process
180 corresponds to the cooccurrence of the decrease in distance between cracks and the increase in
181 the crack aperture. Thus, microcrack evolution can be characterized by the stress level when α

exceeds 1, where the formation of a new crack and crack aperture dilation simultaneously initiates. Based on the above, we estimated the changes in fluid flow characteristics during the fracturing process from the relationship between the permeability and inelastic volumetric strain, equivalent to the crack porosity in this study. Figure 7 shows representative results of the permeability–inelastic volumetric strain curve on a log-log scale. Note that the inelastic volumetric strain (D) was defined here after the stage of elastic deformation (i.e., the onset of dilatancy), where the ratio of D to the ideal elastic volumetric strain (the dashed line in Fig. 5) exceeds 3% (i.e., D=~0.005). The differential stresses at which the slopes exceed 1 are 71.7–77.7% at a confining pressure of 20 MPa while 76.4–94.1% at that of 40 MPa (Figs. 7). These results indicate that above these threshold stresses, the permeability rapidly increases due to the concurrence of new crack formation (i.e., decrease in the distance between cracks) and crack aperture dilation. As shown in Figure 6, the change in permeability deviates from that in the inelastic volumetric strain at around 80% of the maximum stress, which can be caused by both new crack formation and crack aperture opening. Although the slope α ranges from 0 to 1 during the initial stage of inelastic deformation, this reflects the stable crack length increment less contributing to permeability enhancement than the following crack growth.

Considering these results, we propose the deformation stage classifications in terms of the permeability evolution processes (Fig. 8). In addition to the previous model (e.g., Paterson and Wong, 2005), a new stage, the permeability enhancement stage, was newly defined in this study. During *stage I*, a decrease in permeability is attributed to the closure of pre-existing cracks in the direction perpendicular to the maximum principal stress. In this study, the permeability reduction continued until the differential stress reached ~20% of the maximum value (Fig. 3). *Stage II* is a stage of elastic behavior and is characterized by constant permeability. *Stage III* is characterized by a slight permeability increase due to the initiation of the microcracking activity, where this stage begins at ~40% of the maximum differential stress (Fig. 2). When the

differential stress is reached at the crack damage stress (62–77% of the maximum stress), the volumetric strain turns from compression to dilation, indicating the onset of unstable crack growth. The permeability enhancement behavior shows no significant changes yet at this stress. As the differential stress increases further, the changing rate of permeability becomes much larger than that of inelastic volumetric strain before reaching *Stage V* of macroscopic failure. We defined *Stage IV* as the regime of significant permeability enhancement where new crack formation and crack aperture dilation occur. The increase in the confining pressure may inhibit the crack formation and dilation, although both the onset of dilatancy and crack damage stress are less dependent on the confining pressure. The key feature of *stage IV* is dominant in aperture increase, where we assume the new crack formation corresponds to the opening of grain boundaries. On the other hand, *stage III* (the crack initiation stress and crack damage stress) can be characterized by the stable and unstable growth of pre-existing crack length (Bieniawski 1967). The confining pressure is more likely to affect the crack aperture dilation than crack length growth, resulting in the pressure dependence on the onset of *stage IV*. This is also consistent with the experimental evidence that the crack aperture decreases with an increase in confining pressure (Sueyoshi et al., 2020). We note that these experimental results established the new relationship between permeability enhancement and microcracking behavior. To obtain a more detailed permeability model, a quantitative analysis of the effects of geometric factors such as crack connectivity and aperture during deformation is required.

5. Conclusions

This study presents experimental data on the continuous evolution of permeability during triaxial compression. Using nitrogen gas as a pore fluid, we succeeded in measuring the permeability of granite during deformation until failure occurred. In all experiments, as differential stress increased, the permeability initially decreased due to the closure of pre-

existing cracks, and then began to increase at higher differential stress. Although permeability increased by approximately two orders of magnitude during deformation, the variation was larger at 20 MPa than at 40 MPa, suggesting that more cracks developed under the lower confining pressure. Based on the relationship between inelastic volumetric strain and permeability, permeability was controlled mainly by increases in crack porosity during the initial stages of deformation, but a rapid increase in permeability prior to brittle failure was controlled by both new crack formation and crack aperture enhancement. Since the crack aperture is greatly influenced by the confining pressure, the higher the confining pressure, the higher the stress level at which the permeability enhancement stage begins.

Acknowledgments

We thank Tadashi Yokoyama for discussions and technical advice on the experiments. This study was supported by JSPS KAKENHI Grant Numbers 15H02147 and JP16H06476 in Scientific Research on Innovative Areas “Science of Slow Earthquakes”.

Data availability

All datasets obtained or analyzed during this study are presented in this published paper.

References

Baud P., Meredith P. and Townend E., 2012. Permeability evolution during triaxial compaction of an anisotropic porous sandstone, *J. geophys. Res.: Solid Earth*, 117(5), 1–23. https://doi.org/10.1029/2012JB009176

Bernabé, Y., U. Mok, and B. Evans., 2003. Permeability-porosity relationships in rocks subjected to various evolution processes, *Pure appl. Geophys.,* 160(5), 937-960. https://doi.org/10.1007/PL00012574

Bieniawski, Z. T., 1967. Mechanism of brittle fracture of rock: part II—experimental studies. *Int. J. Rock Mech. Min. Sci. Geomech. Abstr.*, **4**(4), 407–423. https://doi.org/10.1016/0148-9062(67)90031-9

Brace W. F., Paulding B. W. and Scholz C., 1966. Dilatancy in the fracture of crystalline rocks, *J. geophys. Res.*, 71(16), 3939–3953. https://doi.org/10.1029/JZ071i016p03939

Brace W. F., Walsh J. B., and Frangos W. T., 1968. Permeability of Granite under High Pressure, *J. geophys. Res.*, 73(6), 2225–2236. https://doi.org/10.1029/JB073i006p02225

Byerlee J. D., 1975. The fracture strength and frictional strength of Weber Sandstone, *Int. J. Rock Mech. Min. Sci.,* 12(1), 1–4. https://doi.org/10.1016/0148-9062(75)90736-6

Fortin J., Stanchits S., Vinciguerra S., and Guéguen, Y., 2011. Influence of thermal and mechanical cracks on permeability and elastic wave velocities in a basalt from Mt. Etna volcano subjected to elevated pressure, *Tectonophysics*, 503(1–2), 60–74. https://doi.org/10.1016/j.tecto.2010.09.028

Gueguen Y. and Dienes J., 1989. Transport Properties of Rocks from Statistics and Percolation, *Math. Geol.*, 21(1), 1–13. https://doi.org/10.1007/BF00897237

Gueguen Y., and Palciauskas V., 1994. *Introduction to the Physics of Rocks*, Press, Princeton, N.J.

Kudo Y., Sano O., Murashige N., Mizuta Y. and Nakagawa K., 1992. Stress-induced crack path in Aji granite under tensile stress, *Pure appl. Geophys.*, 138(4), 641–656. https://doi.org/10.1007/BF00876342

Lei, Xinglin., 2006. Typical phases of pre-failure damage in granitic rocks under differential compression, *Geological Society, London, Special Publications,* 261(1), 11-29. https://doi.org/10.1144/GSL.SP.2006.261.01.02

Mitchell T. M., and Faulkner D. R., 2008. Experimental measurements of permeability evolution during triaxial compression of initially intact crystalline rocks and implications

for fluid flow in fault zones, *J. geophys. Res.: Solid Earth,* 113(11), 1–16. https://doi.org/10.1029/2008JB005588

Paterson, Mervyn S., and Teng-fong Wong., 2005. *Experimental rock deformation-the brittle field*, Springer Science & Business Media.

Scholz C. H., 1968. Microfracturing and the inelastic deformation of rock in compression, *J. geophys. Res.,* 73(4), 1417-1432. https://doi.org/10.1029/JB073i004p01417

Shapiro S. a., Huenges E., and Borm G., 1997. Estimating the crust permeability from fluid-injection-induced seismic emission at the KTB site, *Geophys. J. Int.,* 131(2), F15–F18. https://doi.org/10.1111/j.1365-246X.1997.tb01215.x

Sibson R. H., 1996. Structural permeability of fluid-driven fault-fracture meshes, *J. Struct. Geol.,* 18(8), 1031–1042. https://doi.org/10.1016/0191-8141(96)00032-6

Sueyoshi, Kazumasa, Tadashi Yokoyama, and Ikuo Katayama., 2020. Experimental measurement of the transport flow path aperture in thermally cracked granite and the relationship between pore structure and permeability, *Geofluids,* 2020, 1-10. https://doi.org/10.1155/2020/8818293

Talwani P., and Acree S., 1984. Pore pressure diffusion and the mechanism of reservoir-induced seismicity, *Pure appl. Geophys.*, 122(6), 947–965. https://doi.org/10.1007/978-3-0348-6245-5_14

Tanikawa W., Shimamoto T., Wey S. K., Lin C. W. and Lai W. C., 2008. Stratigraphic variation of transport properties and overpressure development in the Western Foothills, Taiwan, *J. geophys. Res.: Solid Earth*, 113(12), 1–17. https://doi.org/10.1029/2008JB005647

Watanabe T. and Higuchi A., 2015. Simultaneous measurements of elastic wave velocities and electrical conductivity in a brine-saturated granitic rock under confining pressures and their implication for interpretation of geophysical observations, *Prog. Earth Planet. Sci.*, 2(1), 37. https://doi.org/10.1186/s40645-015-0067-0

Yukutake H., 1989. Fracturing Process of Granite Inferred From Measurements of Spatial and Temporal Variations in Velocity During Triaxial Deformations, *J. geophys. Res.*, 94, 15639–15651. https://doi.org/10.1029/JB094iB11p15639

Zhu W. and Wong T., 1997. The transition from brittle faulting to cataclastic flow: Permeability evolution, *J. geophys. Res.: Solid Earth*, 102(B2), 3027–3041. https://doi.org/10.1029/96JB03282

Zoback M. D., and Byerlee J. D., 1975. The effect of microcrack dilatancy on the permeability of Westerly granite, *J. geophys. Res.*, 80(5), 752–755. https://doi.org/10.1029/JB080i005p00752

Figure captions

Figure 1. Overview of the intra-vessel deformation fluid-flow apparatus.

Figure 2. Relationships among differential stress and axial strain (ε_a), radial strain (ε_r), and volumetric strain (ε_v) of Aji granite under confining pressures of 20 and 40 MPa. Compressive strain was taken as positive, and extensional strain as negative.

Figure 3. Evolution of permeability as a function of differential stress under confining pressures of 20 (blue dots) and 40 MPa (red dots). The data points of IVA1389 and IVA1403 represent experiments conducted at a slower deformation rate of 0.02 mm/min. All other data represent experiments conducted at a deformation rate of 0.04 mm/min.

Figure 4. Comparison of our experiment data with those of previous experimental studies. (a) Experimental results at Pc = 40 MPa compared with the data of Zoback and Byerlee's[8] experiment on Westerly granite at an effective pressure of 39 MPa, with permeability

measured by a pulse transient method using argon gas. (b) Experimental results at Pc = 20 MPa compared with the data of Mitchell and Faulkner[10] obtained from Westerly granite at an effective pressure of 20 MPa, with permeability measured by a pore pressure oscillation method using water as a pore fluid.

Figure 5. Typical relationship among differential stress and strains during triaxial compression experiments of Aji granite samples at Pc = 20 MPa. The parameters C, C', and D represent the maximum differential stress, onset of dilatancy, and inelastic volumetric strain, respectively. The dashed line represents the ideal elastic volumetric strain extrapolated form 20–30% of the maximum differential stress.

Figure 6. Inelastic volumetric strain and permeability normalized to the initial values ($k/k_{initial}$) as functions of differential stress normalized to the maximum differential stress at Pc = 20 (a) and 40 MPa (b).

Figure 7. Relationship between permeability normalized to the initial value and inelastic volumetric strain at confining pressures of 20 and 40 MPa. Light blue square: IVA1454; blue circle: IVA1451; light red square: IVA1471; red circle: IVA1428. Note that strains were only measured for these four experiments.

Figure 8. Permeability as a function of inelastic volumetric strain at confining pressure of 20 (a – c) and 40 MPa (d – f). The straight lines represent the lines with slope 1 tangent to the permeability – inelastic volumetric strain curve. The green plots indicate the contact points of the tangent lines with slope 1.

Figure 9. Deformation stages during a triaxial compression test in terms of the permeability evolution. (a) Typical changes in the differential stress normalized by the peak stress and permeability as functions of axial strain at confining pressure of 20 MPa. (b) Schematic illustrations of microcracking characteristics within a sample at each stage.

Table caption

Table 1. Summary of experimental conditions and results.

Pc: confining pressure; $k_{initial}$: initial permeability; k_{max}: permeability at maximum differential stress.

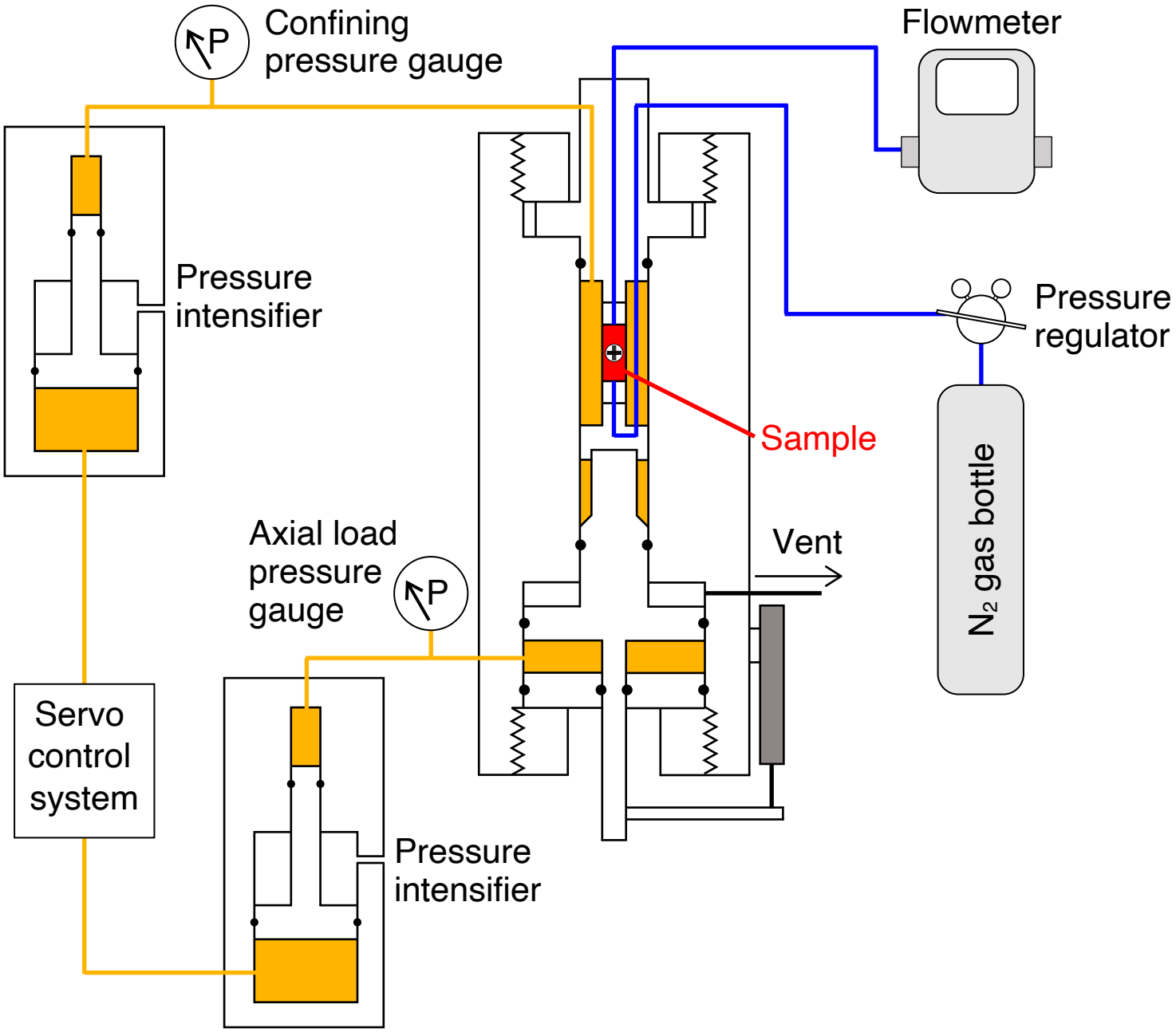
P
Confining pressure gauge
Flowmeter
Pressure intensifier
Pressure regulator
Sample
Axial load pressure gauge
P
Vent
N_2 gas bottle
Servo control system
Pressure intensifier

Figure 1

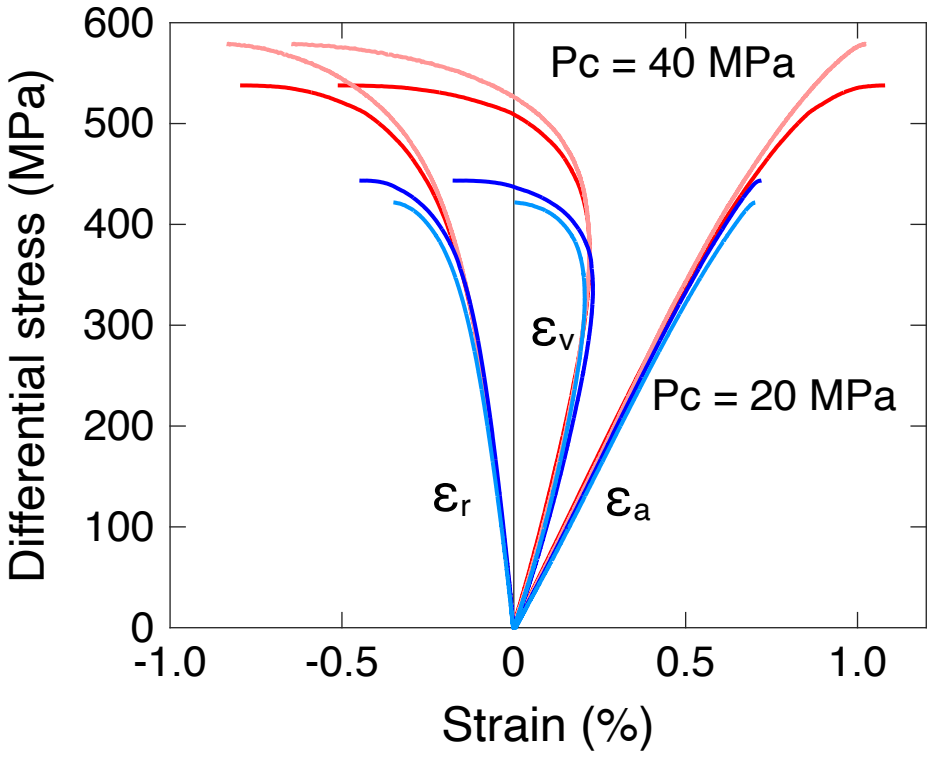
Differential stress (MPa)
600
500
400
300
200
100
0
-1.0
-0.5
0
0.5
1.0
Strain (%)
Pc = 40 MPa
Pc = 20 MPa
εv
εr
εa

Figure 2

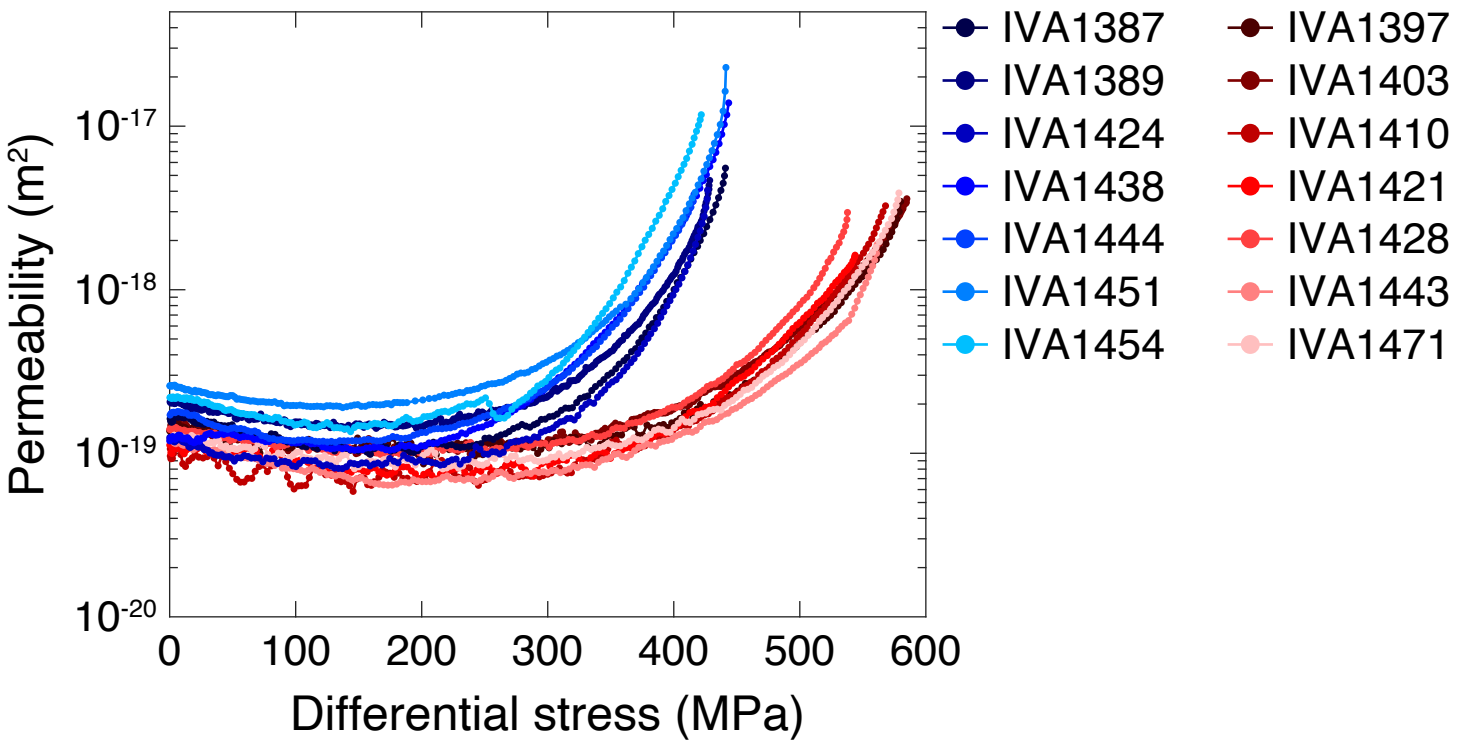
Permeability (m²)
10-17
10-18
10-19
10-20
0
100
200
300
400
500
600
Differential stress (MPa)
IVA1387
IVA1389
IVA1424
IVA1438
IVA1444
IVA1451
IVA1454
IVA1397
IVA1403
IVA1410
IVA1421
IVA1428
IVA1443
IVA1471

Figure 3

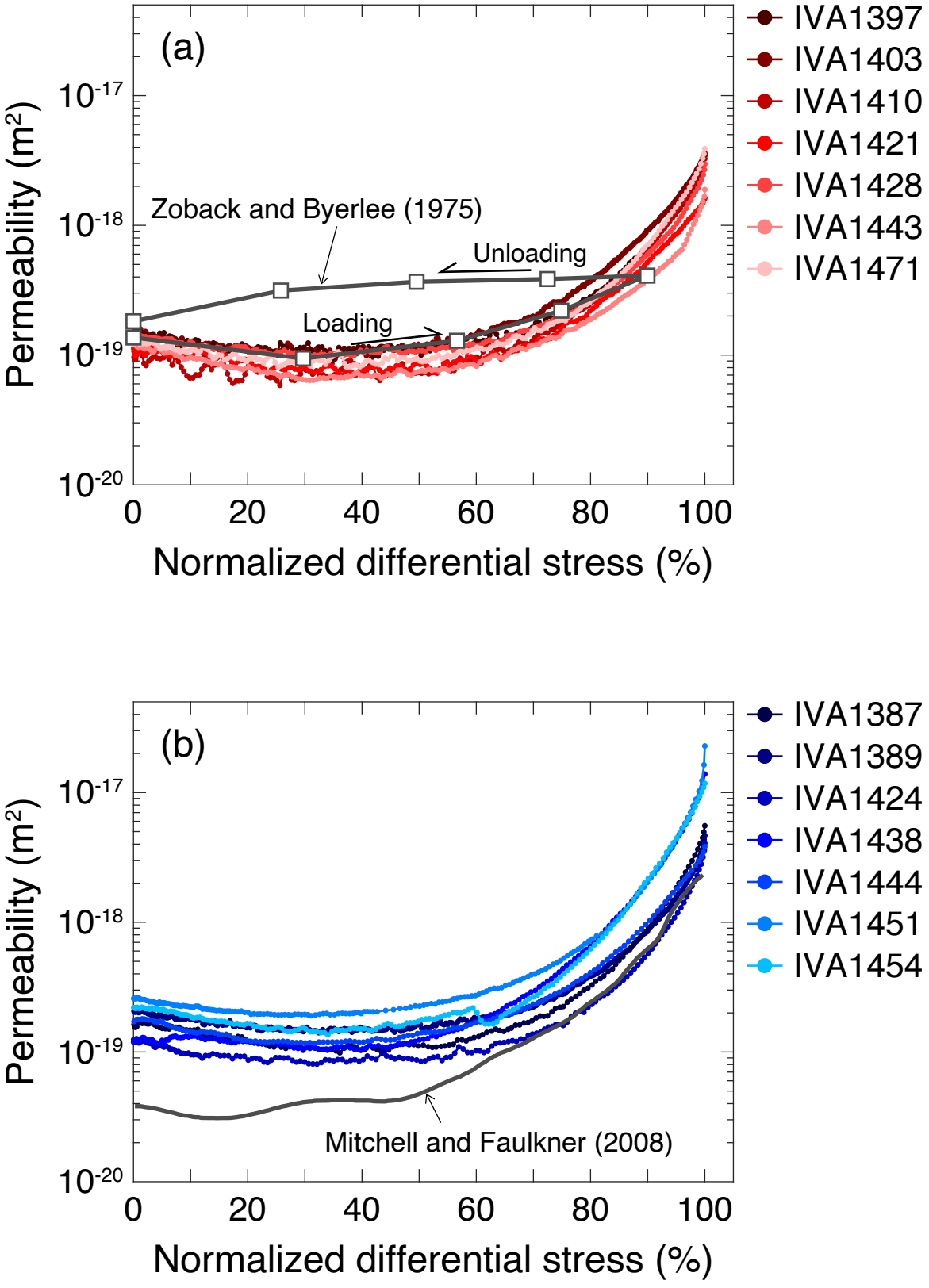
(a)
Permeability (m²)
10-17
10-18
10-19
10-20
Zoback and Byerlee (1975)
Unloading
Loading
0
20
40
60
80
100
Normalized differential stress (%)
IVA1397
IVA1403
IVA1410
IVA1421
IVA1428
IVA1443
IVA1471
(b)
Permeability (m²)
10-17
10-18
10-19
10-20
Mitchell and Faulkner (2008)
0
20
40
60
80
100
Normalized differential stress (%)
IVA1387
IVA1389
IVA1424
IVA1438
IVA1444
IVA1451
IVA1454

Figure 4

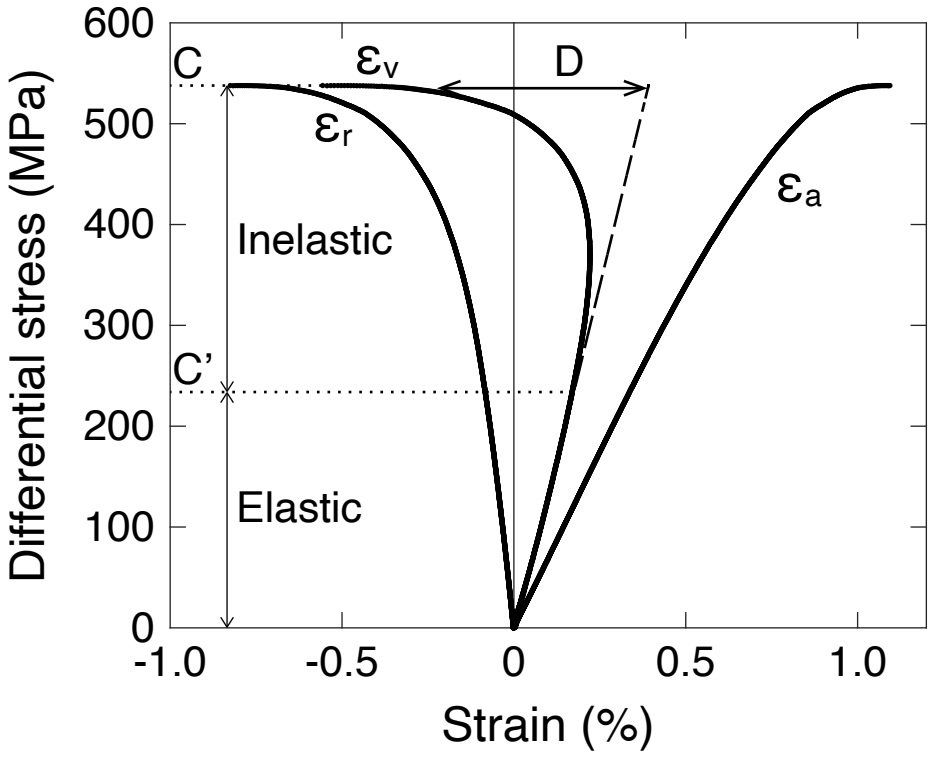
600
500
400
300
200
100
0
C
C'
ε_v
ε_r
ε_a
D
Inelastic
Elastic
-1.0
-0.5
0
0.5
1.0
Differential stress (MPa)
Strain (%)

Figure 5

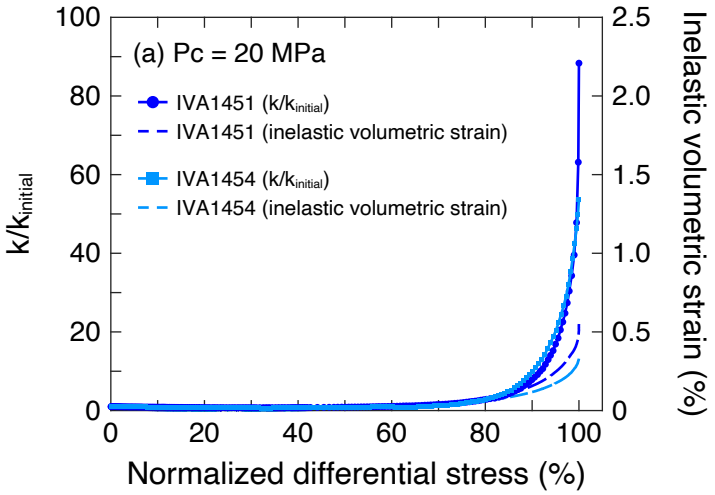
(a) Pc = 20 MPa
IVA1451 (k/k$_{initial}$)
IVA1451 (inelastic volumetric strain)
IVA1454 (k/k$_{initial}$)
IVA1454 (inelastic volumetric strain)
k/k$_{initial}$
Inelastic volumetric strain (%)
Normalized differential stress (%)
0
20
40
60
80
100
0
0.5
1.0
1.5
2.0
2.5

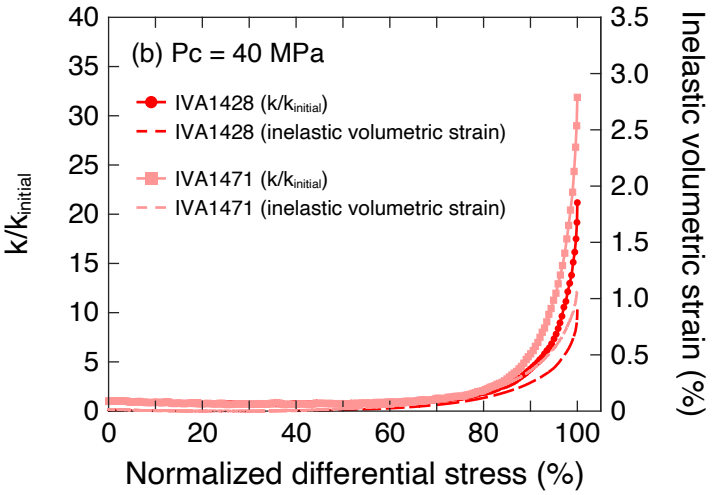
(b) Pc = 40 MPa
IVA1428 (k/k$_{initial}$)
IVA1428 (inelastic volumetric strain)
IVA1471 (k/k$_{initial}$)
IVA1471 (inelastic volumetric strain)
k/k$_{initial}$
Inelastic volumetric strain (%)
Normalized differential stress (%)
0
5
10
15
20
25
30
35
40
0
0.5
1.0
1.5
2.0
2.5
3.0
3.5

Figure 6

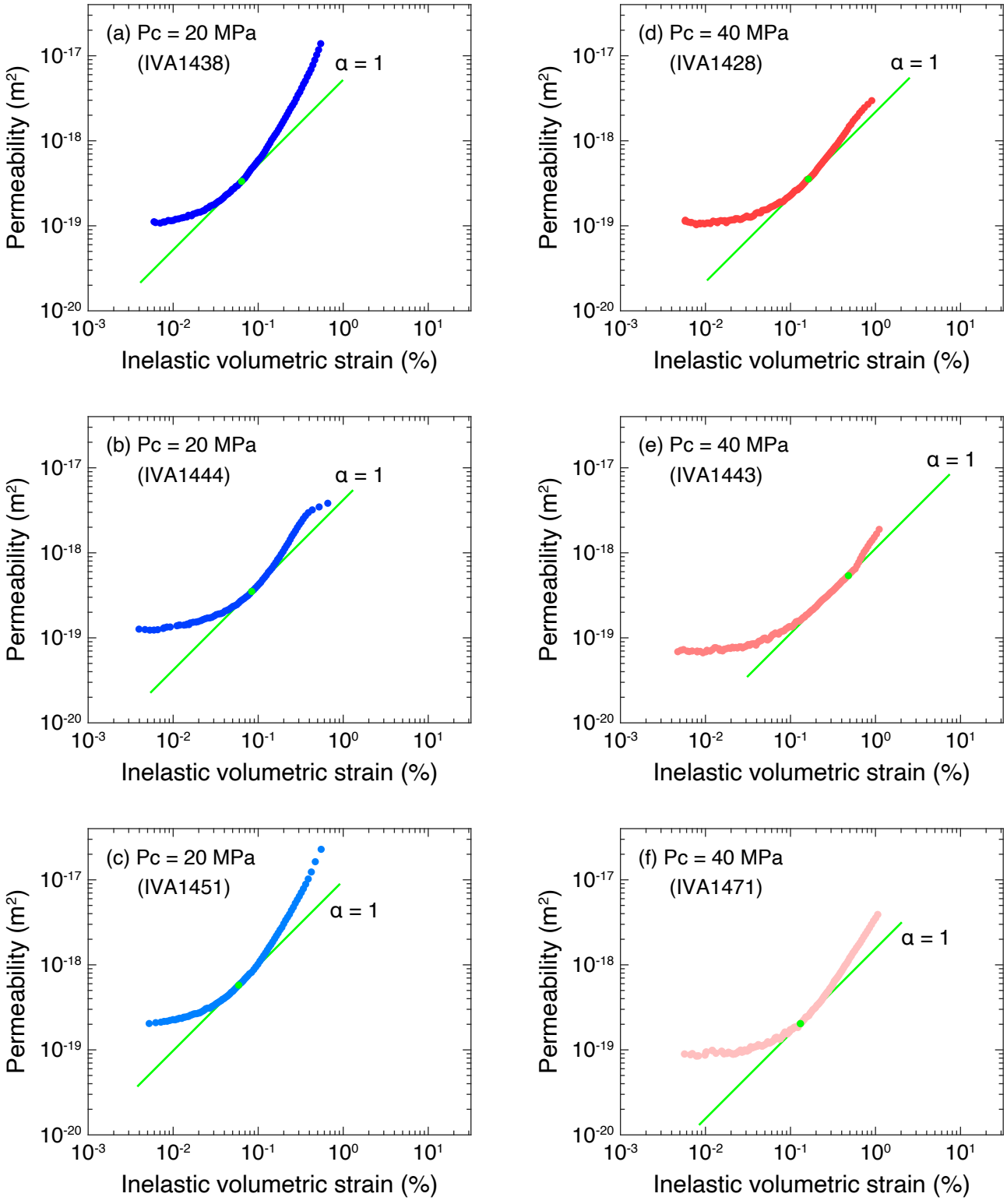
(a) Pc = 20 MPa
(IVA1438)
α = 1
(d) Pc = 40 MPa
(IVA1428)
α = 1
(b) Pc = 20 MPa
(IVA1444)
α = 1
(e) Pc = 40 MPa
(IVA1443)
α = 1
(c) Pc = 20 MPa
(IVA1451)
α = 1
(f) Pc = 40 MPa
(IVA1471)
α = 1
Permeability (m²)
Inelastic volumetric strain (%)

Figure 7

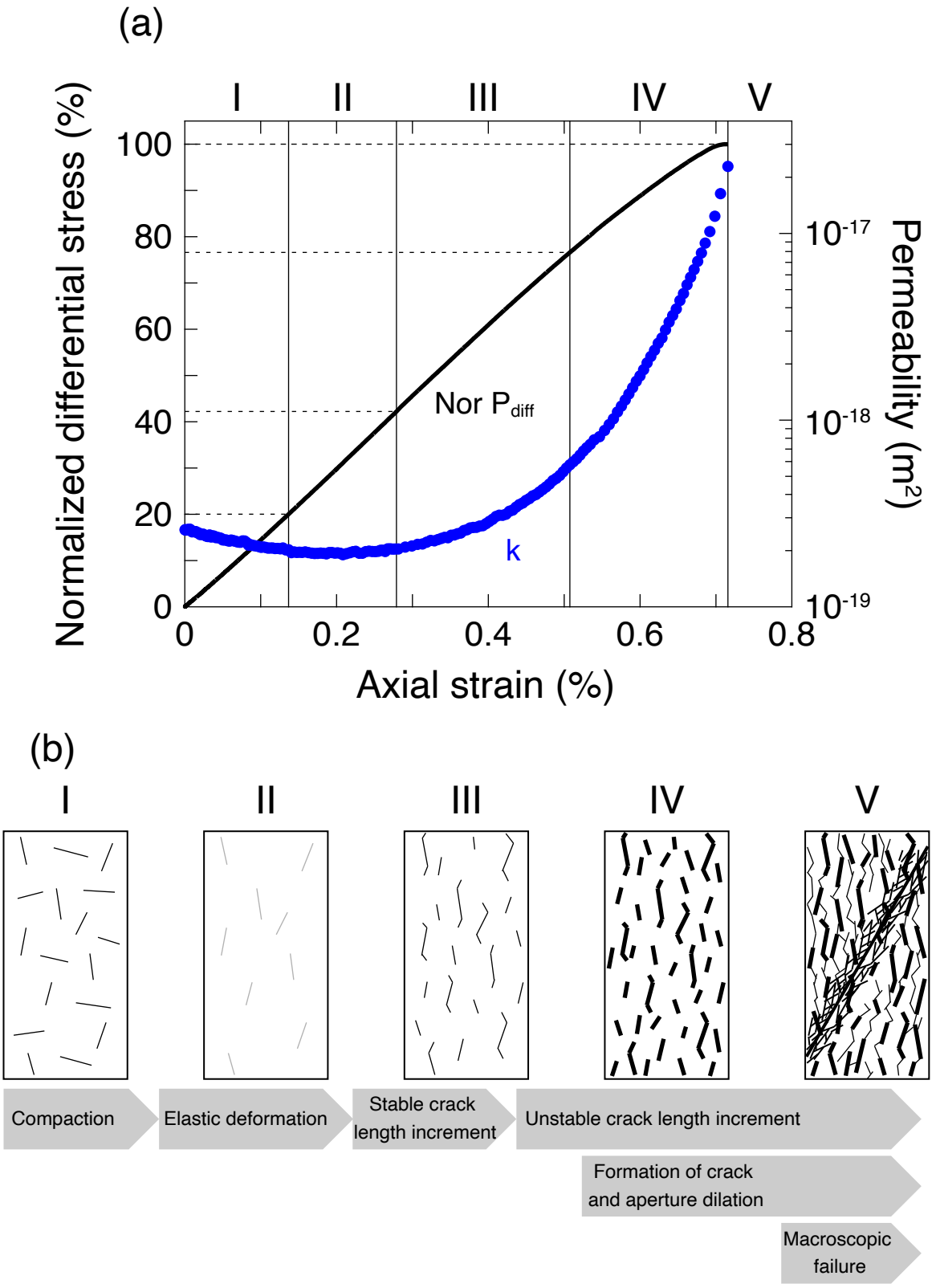
(a)
I
II
III
IV
V
Normalized differential stress (%)
100
80
60
40
20
0
Nor P_diff
k
10^-17
10^-18
10^-19
Permeability (m^2)
0
0.2
0.4
0.6
0.8
Axial strain (%)
(b)
I
II
III
IV
V
Compaction
Elastic deformation
Stable crack length increment
Unstable crack length increment
Formation of crack and aperture dilation
Macroscopic failure

Figure 8

Table 1. Summary of experimental conditions and results

No.	Pc	Displacement rate	Onset of dilatancy		Crack damage stress		Onset of *stage IV*		Maximum differential stress	$k_{initial}$	k_{max}
	(MPa)	(mm/min)	MPa	%	MPa	%	MPa	%	(MPa)	(m^2)	(m^2)
IVA1387	20	0.04							441	1.63×10^{-19}	5.54×10^{-18}
IVA1389	20	0.02							428	2.06×10^{-19}	4.66×10^{-18}
IVA1424	20	0.04	162	37.9	265	62.1			427	1.25×10^{-19}	4.06×10^{-18}
IVA1438	20	0.04	187	42.2	302	68.2	318	71.7	444	1.19×10^{-19}	1.39×10^{-17}
IVA1444	20	0.04	176	42.3	282	67.8	323	77.7	416	1.71×10^{-19}	3.83×10^{-18}
IVA1451	20	0.04	186	42.2	330	74.7	338	76.6	441	2.59×10^{-19}	2.28×10^{-17}
IVA1454	20	0.04	176	41.6	326	77.3			422	2.19×10^{-19}	1.17×10^{-17}
IVA1397	40	0.04							580	1.37×10^{-19}	3.47×10^{-18}
IVA1403	40	0.02							585	1.48×10^{-19}	3.60×10^{-18}
IVA1410	40	0.04							568	1.06×10^{-19}	3.26×10^{-18}
IVA1421	40	0.04							544	1.12×10^{-19}	1.63×10^{-18}
IVA1428	40	0.04	234	43.5	370	68.7	453	84.2	538	1.40×10^{-19}	2.97×10^{-18}
IVA1443	40	0.04	213	38.0	362	64.6	528	94.1	561	1.21×10^{-19}	1.89×10^{-18}
IVA1471	40	0.04	234	40.3	374	64.6	443	76.4	579	1.22×10^{-19}	3.90×10^{-18}

Pc, confining pressure; $k_{initial}$, initial permeability; k_{max}, permeability at maximum differential stress.